

# Lawrence Berkeley National Laboratory

## Recent Work

### Title

Characterization of Photo-Induced Charge Transfer and Hot Carrier Relaxation Pathways in Spinel Cobalt Oxide (Co O )

### Permalink

<https://escholarship.org/uc/item/6533q0wf>

### Journal

The Journal of Physical Chemistry C, 118(39)

### ISSN

1932-7447

### Authors

Jiang, Chang-Ming  
Baker, L. Robert  
Lucas, J. Matthew  
et al.

### Publication Date

2014-10-02

# Characterization of Photo-Induced Charge Transfer and Hot Carrier Relaxation Pathways in Spinel Cobalt Oxide ( $\text{Co}_3\text{O}_4$ )

Chang-Ming Jiang<sup>†</sup> // <sup>⊥</sup>, L. Robert Baker<sup>†</sup>, J. Matthew Lucas<sup>‡</sup>, Josh Vura-Weis<sup>†</sup>, A. Paul Alivisatos<sup>†</sup> <sup>⊥</sup>, and Stephen R. Leone<sup>†</sup> <sup>§</sup> // <sup>\*</sup>

<sup>†</sup> Department of Chemistry, <sup>‡</sup> Department of Mechanical Engineering, and

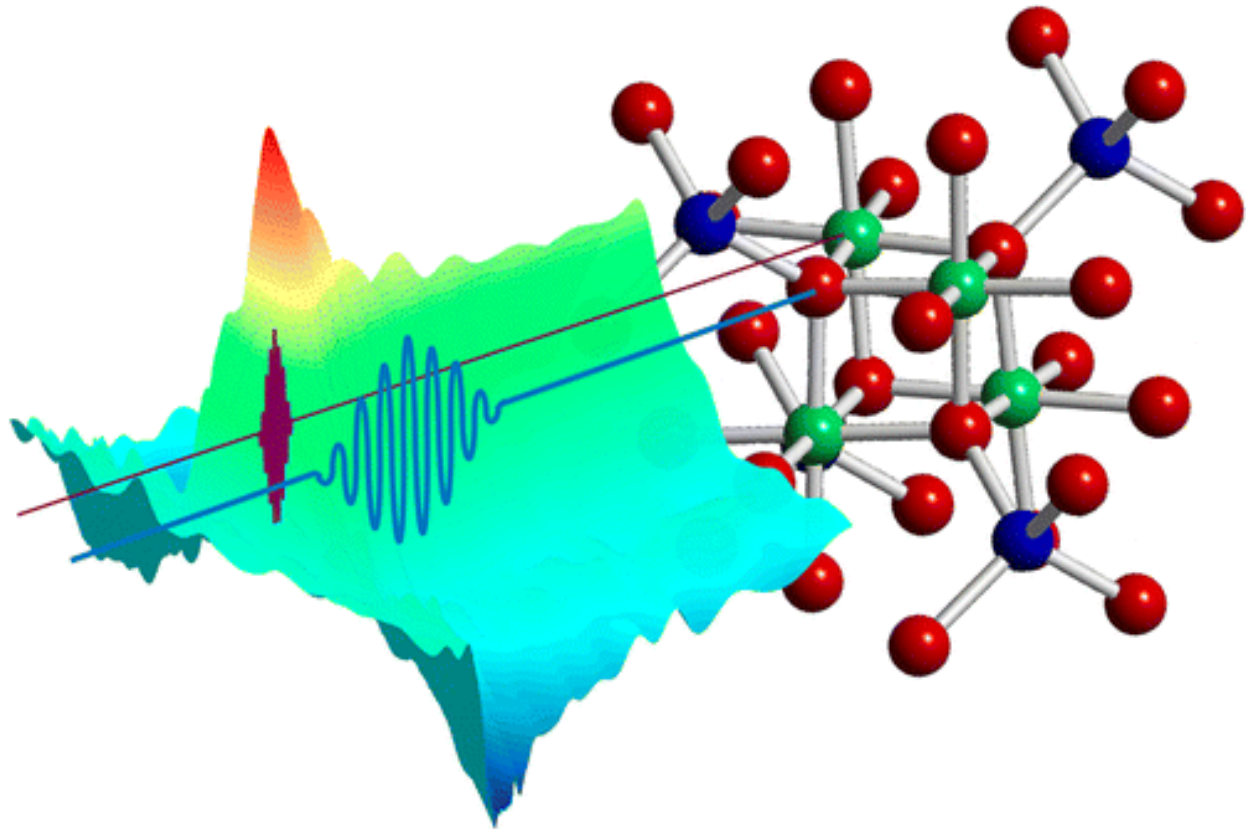
<sup>§</sup> Department of Physics, University of California, Berkeley, California 94720, United States

<sup>⊥</sup> Chemical Sciences Division and <sup>⊥</sup> Materials Sciences Division, Lawrence Berkeley National Laboratory, Berkeley, California 94720, United States

DOI: 10.1021/jp5071133

\*Phone: (510) 643-5467; fax: (510) 643-1376; e-mail: srl@berkeley.edu.

## Abstract



The identities of photoexcited states in thin-film  $\text{Co}_3\text{O}_4$  and the ultrafast carrier relaxation dynamics of  $\text{Co}_3\text{O}_4$  are investigated with oxidation-state-specific pump–probe femtosecond core level spectroscopy. A thin-film sample is excited near the 2.8 eV optical absorption peak, and the resulting spectral changes at the

58.9 eV  $M_{2,3}$ -edge of cobalt are probed in transient absorption with femtosecond high-order harmonic pulses generated by a Ti/sapphire laser. The initial transient state shows a significant 2 eV redshift in the absorption edge compared to the static ground state, which indicates a reduction of the cobalt valence charge. This is confirmed by a charge transfer multiplet spectral simulation, which finds the experimentally observed extreme ultraviolet (XUV) spectrum matches the specific  $O^{2-}(2p) \rightarrow Co^{3+}(e_g)$  charge-transfer transition, out of six possible excitation pathways involving  $Co^{3+}$  and  $Co^{2+}$  in the mixed-valence material. The initial transient state has a power-dependent amplitude decay ( $190 \pm 10$  fs at  $13.2$  mJ/cm<sup>2</sup>) together with a slight redshift in spectral shape ( $535 \pm 33$  fs), which are ascribed to hot carrier relaxation to the band edge. The faster amplitude decay is possibly due to a decrease of charge carrier density via an Auger mechanism, as the decay rate increases when more excitation fluence is used. This study takes advantage of the oxidation-state-specificity of time-resolved XUV spectroscopy, further establishing the method as a new approach to measure ultrafast charge carrier dynamics in condensed-phase systems.

•

## 1 Introduction

Transition-metal oxides have received much attention as photocatalysts and interlayer materials in photovoltaics, especially because of their good earth-abundance, stability, and controllable band gap and charge carrier properties.(1, 2) Unlike covalent semiconductor materials such as Si, Ge and GaAs, transition-metal oxides possess a greater ionic bonding character and a localized electronic structure, thus exhibiting a wide range of important catalytic and semiconductor properties. Not only are the synthetic methods and applications of transition-metal oxide-based materials and nanomaterials extensively developed,(3-5) conceptual principles in terms of electronic structure and charge carrier dynamics within these materials have also been studied.(6-9) Understanding these concepts, including d-electron behavior, hot carrier relaxation, and interfacial charge transfer, is important for developing highly efficient photovoltaic and photocatalytic devices.

In most transition-metal oxides, the d orbitals are partially filled and split between two bands separated by a d–d Coulomb repulsion energy  $U$ , such that electron hopping between metal sites requires energy. On the other hand, charge conduction in metal oxides can also occur through electron transfer from the oxygen ligand to the metal cation, which is defined by a charge transfer band gap  $\Delta$ . As a result, in transition-metal oxides, the conduction band consists mostly of empty metal d orbitals, while the valence band has both oxygen 2p and metal d orbital characteristics. Whether or not the charge transfer gap  $\Delta$  is larger than the d–d repulsion  $U$  defines two different types of semiconductors: Mott–Hubbard ( $U < \Delta$ ) and charge-transfer semiconductor ( $U > \Delta$ ). (10) In the case of transition-metal fluorides, a continuous transition from Mott–Hubbard to charge-transfer

semiconductor has been observed across the first-row transition metals.(11) If the composition is changed from fluorine to oxygen, however, considering the electronegativity difference alone is not sufficient to define the type of semiconductor, because of the larger extent of orbital mixing through interatomic covalent bonding in the oxide compounds. Among various transition-metal oxides, the thermodynamic stability and surface redox reactivity make cobalt oxide ( $\text{Co}_3\text{O}_4$ ) an important catalyst for CO oxidation,(12) Fischer–Tropsch synthesis,(13) cyclohexane dehydrogenation,(14) and the oxygen evolution reaction in water splitting.(15)  $\text{Co}_3\text{O}_4$  doped with other elements (F, Ni, or alkali metals) also exhibits enhancements in specific properties.(16-18)  $\text{Co}_3\text{O}_4$  has a spinel structure ( $\text{AB}_2\text{O}_4$ ) in which oxygen ions form a face centered cubic (fcc) lattice, and two different cobalt oxidation states,  $\text{Co}^{2+}$  and  $\text{Co}^{3+}$ , respectively, occupy tetrahedral and octahedral symmetry sites with a 1:2 stoichiometric ratio (Figure 1A). Because of the presence of two cobalt oxidation states and d-electron configurations, the electronic structure of  $\text{Co}_3\text{O}_4$  has even more complexity than other transition-metal oxides. Each  $\text{Co}^{2+}$  ion has a high-spin  $^4\text{A}_2$  configuration and three unpaired electrons in  $t_2$  orbitals, while for the  $\text{Co}^{3+}$  ion, the d electrons of the low-spin  $^1\text{A}_1$  configuration are all paired in  $t_{2g}$  orbitals. Density functional theory (DFT) calculation(19) has suggested that the conduction band of  $\text{Co}_3\text{O}_4$  is mainly composed of the  $\text{Co}^{2+} t_2$  minority spin orbitals and the  $\text{Co}^{3+} e_g$  orbitals. The valence band has contributions from filled d orbitals of both cobalt oxidation states as well as 2p orbitals of the oxygen anion with some extent of hybridization effects between these orbitals.

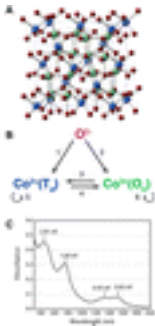


Figure 1. (A) Illustration of the crystal structure of spinel  $\text{Co}_3\text{O}_4$ . Red: oxygen fcc sublattice. Blue:  $\text{Co}^{2+}$  ions occupying tetrahedral sites. Green:  $\text{Co}^{3+}$  ions occupying octahedral sites. (B) Six possible optical excitation pathways in  $\text{Co}_3\text{O}_4$ , which consists of  $\text{O}^{2-}$  anions and two different cobalt oxidation states ( $\text{Co}^{2+}$  and  $\text{Co}^{3+}$ ). There are two ligand-to-metal-charge-transfer pathways (1 and 2), two metal-to-metal-charge-transfer pathways (3 and 4) and two local d–d ligand field excitations (5 and 6). (C) UV/visible absorption spectrum of thin-film  $\text{Co}_3\text{O}_4$  on a

quartz substrate prepared by the same procedure as described in the [Experimental Methods](#) section.

Considering the composition of spinel  $\text{Co}_3\text{O}_4$ , six possible electronic transitions can occur when absorbing a photon at an energy higher than the band gap (Figure 1B): these include two ligand-to-metal-charge-transfer (LMCT) pathways from O 2p to the two types of cobalt cations, two metal-to-metal-charge-transfer (MMCT) transitions between different cobalt oxidation states, and one d–d ligand field excitation within each of the  $\text{Co}^{2+}$  and  $\text{Co}^{3+}$  cations. Although the spatial overlap between two d orbitals of separated cobalt cations seems to be small, a MMCT transition can still occur across an oxygen bridge if both d orbitals have significant bonding characters with the same O 2p orbital. High-pressure-induced MMCT in  $\text{Co}_3\text{O}_4$  from  $\text{Co}^{2+}$  to  $\text{Co}^{3+}$  has been observed experimentally, transforming the lattice structure from normal spinel to inverse spinel.<sup>(20)</sup> All the LMCT and MMCT pathways involve cobalt oxidation state changes at one or both lattice sites, while d–d excitations only modify the local electronic configuration without affecting the oxidation state of the cobalt ions.

The visible/IR absorption spectrum of  $\text{Co}_3\text{O}_4$  shows four distinguishable peaks at 0.8, 0.9, 1.6, and 2.8 eV;<sup>(21)</sup> however, there has been little success in assigning electronic transitions to these absorption peaks. Molecular orbitals in the presence of a ligand field have been constructed for an entire unit cell, and available transitions are compared with the visible/IR absorption peaks.<sup>(22)</sup> With this approach, the 2.8 eV peak is assigned to the  $\text{O}^{2-}(2p) \rightarrow \text{Co}^{3+}(e_g)$  transition.

Experimental interpretation has been made by monitoring the absorption spectrum changes as  $\text{Co}^{2+}$  in tetrahedral sites are gradually substituted by  $\text{Zn}^{2+}$ .<sup>(23)</sup> That work suggests the broad peak at 2.8 eV actually consists of two transitions, and the lower and higher energy shoulders correspond to  $\text{O}^{2-}(2p) \rightarrow \text{Co}^{2+}(t_2)$  and  $\text{O}^{2-}(2p) \rightarrow \text{Co}^{3+}(e_g)$  charge transfer, respectively. Nevertheless, no direct observation and assignment of photoexcited states of  $\text{Co}_3\text{O}_4$  have been published. Understanding how  $\text{Co}_3\text{O}_4$  interacts with visible photons, including the identity of the initially photoinduced excited state and the subsequent carrier relaxation, can provide insightful explanations for the photocatalytic activity of the material.

Time-resolved spectroscopy has been widely used to study ultrafast photophysical or photochemical processes following photon absorption. However, one common problem when applied to the condensed-phase is that the complexity of the electronic structure makes the experimental excited-state spectrum, from the IR to UV region, difficult to interpret. Transitions associated with core levels, usually by probing with X-ray or extreme ultraviolet (XUV) photons, possess unique capabilities to distinguish different elements, oxidation states, local spin states, and covalent/ionic bonding characteristics.<sup>(24-26)</sup>

Taking cobalt oxide as an example, electronic structure changes occurring near cobalt atoms can be observed via the 58.9 eV cobalt  $M_{2,3}$ -edge, which is the  $Co\ 3p\ 3d^n \rightarrow 3p\ 3d^{n+1}$  dipole transition, and the difference between  $Co^{2+}$  and  $Co^{3+}$  can be separated. Moreover, the development of the high harmonic generation (HHG)(27) technique enables conversion of widely available near-IR 800 nm pulses to XUV pulses with durations of femtoseconds(28-30) or even attoseconds.(31, 32) These short pulses can be utilized as an ideal tool for studying ultrafast photochemical processes in transition-metal-containing condensed-phase systems.

Synchrotron light sources can provide high energy X-ray photons to probe transition-metal L-edges, which generally show sharper features than M-edge absorption due to more obvious spin-orbit coupling effects in the  $n = 2$  shell. The energy of photons used to probe L-edges of first-row transition metals (400–1200 eV) can also access the K-edge of the oxygen ligand (~540 eV), which provides the opportunity to study the valence charge distribution around both transition-metal cations and oxygen ligands at once. However, the mass absorption coefficients at the M-edge ( $\sim 10^5\ cm^2/g$ ) are larger than those at the L-edge ( $\sim 10^4\ cm^2/g$ ) by an order of magnitude. This sensitivity makes M-edge absorption in the XUV region especially useful to measure samples at the nanometer scale.

Transient X-ray absorption spectroscopy at the L-edge has been applied to investigate the electronic structure of cuprous oxide,(33) photoinduced spin crossover,(25) excited-state molecular and electronic structure changes(34-36) in transition-metal complexes, and ultrafast spin dynamics in condensed-phase.(37) Coherent optical phonons, ultrafast demagnetization dynamics, and the excited-state character of hematite have also been studied by table-top HHG apparatuses.(38-40)

This work exploits the elemental and oxidation-state specificity of transient XUV spectroscopy. When pumped at 400 nm, the identity of the  $Co_3O_4$  excited state and the subsequent charge carrier relaxation process are resolved. This research provides evidence that 400 nm excitation induces specifically the  $O^{2-}(2p) \rightarrow Co^{3+}(e_g)$  charge transfer transition. Two subpicosecond dynamics time scales are observed after the optical excitation: A  $190 \pm 10$  fs fast lifetime of transient absorbance amplitude decay can be explained as Auger relaxation of extra charge carriers, which is supported by an increased decay rate with higher excitation fluences. An additional  $\sim 300$  meV spectral redshift that occurs in  $535 \pm 33$  suggests hot carriers undergo relaxation toward the band edge via carrier-phonon scattering.

•

## 2 Experimental Methods

This research aims to study ultrafast charge carrier dynamics of thin-film  $Co_3O_4$  following femtosecond 400 nm visible excitation. Changes of electronic structures

after excitation are probed by measuring XUV transient absorption differences. The apparatus (Figure 2) consists of an 800 nm Ti/sapphire laser to generate high-order harmonics as the probe and to produce frequency-doubled pulses for the pump excitation, a high vacuum system with high harmonic source, toroidal focusing mirror, raster scanned sample, a variable line space grating, and an X-ray charge-coupled device (CCD) camera for spectral detection after the sample.



Figure 2. Layout of the transient XUV absorption instrument. High harmonics are generated in a semi-infinite gas cell (SIGC) with a two-color laser driver field (1.8 mJ, 40 fs at 800 nm +20  $\mu$ J, 60 fs at 400 nm). The neon pressure in the SIGC is 100 Torr ( $1.3 \times 10^4$  Pascals). The residual 800/400 nm driver pulses are blocked by a 0.6  $\mu$ m Al foil. The 400 nm pump beam is frequency-doubled from 800 nm near-IR, and the pump energy is reduced by a variable neutral density filter (VND). The instrument has to be under high vacuum ( $\sim 10^{-7}$  Torr) beyond the semi-infinite gas cell because air is highly absorptive to XUV photons.

Cobalt oxide thin-film samples are prepared by RF magnetron sputtering of  $\sim 10$  nm cobalt metal on 100 nm  $\text{Si}_3\text{N}_4$  substrates, followed by oxidation in ambient atmosphere in a tube furnace at 500  $^\circ\text{C}$  for 1 h and cooling naturally to room temperature. The actual sample thickness is not directly measured, but it is estimated by scaling the resonant  $M_{2,3}$ -edge absorption amplitude with the XUV absorption cross section provided by the CXRO.<sup>(41)</sup> Four absorption peaks (0.82, 0.93, 1.64, and 2.81 eV) appear in visible/IR absorption spectra of thin-film  $\text{Co}_3\text{O}_4$  on a quartz substrate prepared by the same procedures (Figure 1C), which agree with the literature values.<sup>(21)</sup> The composition and phase of spinel  $\text{Co}_3\text{O}_4$  are confirmed by selected area electron diffraction (Figure S1, [Supporting Information](#)). Micro-Raman measurement shows four distinct Raman shift peaks (474, 518, 611, and 679  $\text{cm}^{-1}$ ) (refer to Figure S2, [Supporting Information](#)) that match reported signatures of spinel  $\text{Co}_3\text{O}_4$ .<sup>(42)</sup> Similarly, measurements were also made to confirm that the pump beam does not damage samples after each pump–probe measurement.

The Ti/sapphire chirped pulse amplifier (Spitfire Pro, Spectra Physics) provides 3.5 mJ pulses spectrally centered at 800 nm at a 1 kHz repetition rate. HHG is accomplished by splitting and focusing  $\sim 1.8$  mJ of the near-IR fundamental pulses into a 40 cm long semi-infinite gas cell (SIGC) filled with 100 Torr ( $\sim 1.3 \times 10^4$  Pascals) of neon. The laser peak intensity is  $5.7 \times 10^{14}$   $\text{W}/\text{cm}^2$  at the 100  $\mu$ m diameter focus. About 20  $\mu$ J of 400 nm light is mixed into the fundamental pulses in order to generate both odd- and even-order harmonics by breaking the electric field symmetry, so that the XUV photons will have more uniform spectral coverage. The use of a SIGC simplifies the alignment procedure of the high harmonic source and is able to generate XUV pulses with higher efficiency

because of its longer interaction region compared to other short path length HHG geometries.<sup>(43)</sup> The generated XUV pulses are used as a probe beam and possess  $\sim 2 \times 10^{-10}$  J energy per pulse. After refocusing by a gold-coated toroidal mirror, the beam size of the XUV probe at the sample location is about 80  $\mu\text{m}$ . The pump beam is generated by frequency-doubling to 400 nm (fwhm  $\approx 11$  nm, refer to Figure S3, [Supporting Information](#)) the rest of the split near-IR pulse energy in a 100  $\mu\text{m}$  thick type-I  $\beta\text{-BaB}_2\text{O}_4$  (BBO) crystal. A variable neutral density filter controls the pump beam power, which is focused to a spot size of 150  $\mu\text{m}$  diameter on the sample and adjusted to an average power between 0.86 and 2.70 mW at 1 kHz for the pump fluence dependence studies. On the basis of the size of the pump beam and the sample absorbance at 400 nm ( $\sim 0.45$ , refer to Figure 1C), this is equivalent to 4.87–15.3  $\text{mJ}/\text{cm}^2$  fluence and  $3$  to  $9 \times 10^{21} \text{ cm}^{-3}$  excited charge carrier density. After transmitting through the  $\text{Co}_3\text{O}_4$  sample supported by the  $\text{Si}_3\text{N}_4$  substrate, the XUV pulses are spectrally dispersed by a variable line-spacing grating onto a CCD camera (PIXIS-400, Princeton Instruments). On one 20  $\mu\text{m} \times 20 \mu\text{m}$  camera pixel, average photon counts are about  $2 \times 10^4$  per second, and the energy range of the spectrometer is from 38 to 80 eV with  $\sim 150$  meV spectral resolution. The apparatus combines the spectrometer located after the sample and the broadband nature of XUV pulses (50–72 eV, Figure S4, [Supporting Information](#)) generated by HHG, to efficiently record transient spectra at multiple photon energies at once. The temporal resolution of the apparatus is limited by the  $\sim 40$  fs pump beam duration. Pump–probe traces are taken by varying a delay stage in the pump beam path and a mechanical shutter controlling the pump beam passage. At each pump–probe delay time, the differential optical density spectra are obtained by dividing alternating transmitted XUV spectra with pump beam on/off for 2 s each. The 3 mm  $\times$  3 mm sample is raster-scanned by 100  $\mu\text{m}$  spatial step sizes between individual pump–probe data acquisition, such that each transient spectrum is taken at an unused sample spot. Spectra at 500 fs before time-zero (probe beam arrives prior to pump beam) are subtracted from spectra taken at every pump–probe delay in order to eliminate the artifacts of residual scattered light from the pump beam. Transient absorbance spectra at each individual pump–probe delay are averaged over 56 runs. Errors resulting from pump and probe beam fluctuations are less than 1% while the maximum differential absorbance signal is 20%. Electron diffraction shows that less than 10% of CoO is formed after four repeated pump–probe measurements at 2.33 mW average pump power (Figure S1, [Supporting Information](#)). The heating effect by the pump pulses is believed to cause this sample reduction in a high vacuum environment; however, the extent of this effect should not alter the acquired XUV transient spectra.

•

### 3 Results and Discussion

#### 3.1 Static XUV Absorption Spectrum and Fitting Results

Figure 3 shows the resonant absorption edge of a thin-film  $\text{Co}_3\text{O}_4$  sample. The resonant absorption near 60 eV indicates the  $\text{Co } 3p \rightarrow 3d$  transition, which demonstrates the elemental specificity of X-ray spectroscopy. The nonresonant absorption contributions extending from the valence electron ionization at  $\sim 20$  eV have been subtracted from the raw spectrum. By scaling the amplitude of this cobalt  $M_{2,3}$ -edge with the absorption cross section available on CXRO,(41) the thickness of the sample is approximated to be 22 nm. When comparing with the  $\alpha\text{-Fe}_2\text{O}_3$  M-edge absorption,(40)  $\text{Co}_3\text{O}_4$  clearly exhibits a broader feature starting from 58 eV and extending above 70 eV. This is likely due to the existence of both  $\text{Co}^{2+}$  and  $\text{Co}^{3+}$  in the material.

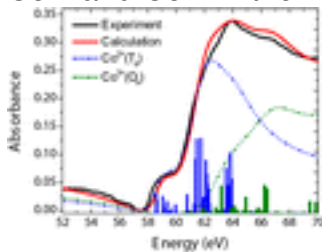


Figure 3. Static M-edge absorption spectrum of  $\text{Co}_3\text{O}_4$  in the XUV region. Black line: experimental spectrum. Red line: spectrum calculated by charge transfer multiplet model. Blue sticks and dashed line: tetrahedrally coordinated  $\text{Co}^{2+}$  absorption contribution. Green sticks and dashed line: octahedrally coordinated  $\text{Co}^{3+}$  absorption contribution. The 1:2  $\text{Co}^{2+}/\text{Co}^{3+}$  stoichiometric ratio has been accounted for.

This static absorption spectrum is fitted with the charge transfer multiplet model by using the program CTM4XAS55.(44, 45) Calculated  $\text{Co}^{2+}$  and  $\text{Co}^{3+}$  absorptions correspond to  $3d^7 ({}^4 A_2) \rightarrow 3p^5 3d^8$  and  $3d^6 ({}^1 A_1) \rightarrow 3p^5 3d^7$  transitions, respectively, followed by adding up the individual absorptions of  $\text{Co}^{2+}$  and  $\text{Co}^{3+}$  ions with 1:2 stoichiometric ratios. When calculating the multiplet effect resulting from the d–d electrostatic interaction, Slater integrals  $F^2$ ,  $F^4$ ,  $G^1$ , and  $G^3$  are reduced to 60% of the atomic parameters empirically in order to account for the configuration–interaction effect. On the basis of the actual spinel crystal structure,  $\text{Co}^{2+}$  is given tetrahedral ligand field symmetry in the calculation with a ligand field splitting energy between e and  $t_2$  orbitals, termed 10 Dq, equal to 0.3 eV, while  $\text{Co}^{3+}$  ion is located in a 10 Dq = 1.8 eV octahedral field. These ligand field parameters, as well as the charge transfer parameter used to account for the orbital mixing between metal ions and surrounding oxygen ligands, are identical to those values used to fit the L-edge absorption spectrum of  $\text{Co}_3\text{O}_4$  by Morales et al.(46) The amplitude integral of allowed transitions is then normalized to the number of d-electron vacancies (3 and 4 for  $\text{Co}^{2+}$  and  $\text{Co}^{3+}$ , respectively). To give

a best match to the experimental data, the calculated stick spectra are broadened by a Lorentzian line width  $L_{\min}$  below a certain onset energy  $E_{\text{onset}}$  and an increasing Lorentzian line width  $\Gamma = L_{\min} + dL^*(E - E_{\text{onset}})$  above the onset energy. This variable Lorentzian broadening accounts for the term-dependent Auger lifetimes of core-hole excited states, which are generally shorter for higher-energy transitions due to the presence of more decay channels.<sup>(47)</sup> A Fano line shape is then applied to the spectra with a Fano parameter  $q$  in order to account for the interference between the  $3p \rightarrow 3d$  transition and the direct ionization of  $3d$  electrons to the continuum. Finally, a 150 meV Gaussian instrumental broadening is applied to the individual spectra before summing up according to the stoichiometric ratio. Calculation parameters used in CTM4XAS55 and the broadening parameters for  $\text{Co}^{2+}$  and  $\text{Co}^{3+}$  are listed in Table 1. Considering the stoichiometric ratio and the number of d-electron vacancies,  $\text{Co}^{3+}$  should contribute more on the M-edge oscillator strength than  $\text{Co}^{2+}$  although it is not very obvious in Figure 3. This is due to a significant amount of  $\text{Co}^{3+}$  absorption located above the 72 eV aluminum cutoff energy, which is not detectable in the experiment setup.

**Table 1. Calculation and Broadening Parameters Used for Fitting of the  $\text{Co}_3\text{O}_4$  Ground-State M-Edge Absorption Spectrum**

	electronic symmetry	Slater integral <sup>a</sup>	$10 D_q$ (eV)	$L_{\min}^b$ (eV)	$dL^b$	$E_{\text{onset}}^b$ (eV)	$q$
$\text{Co}^{2+}$ ( $T_d$ )	high spin: $A_2^4$	0.60	0.3	0.1	0.42	55.8	2.7
$\text{Co}^{3+}$ ( $O_h$ )	low spin: $A_1^1$	0.60	1.9	0.1	0.42	56.3	1.7

<sup>a</sup>Ratio relative to atomic parameters.

<sup>b</sup>The variable Lorentzian line width  $\Gamma$  is approximated by the formula  $\Gamma = L_{\min} + dL^*(E - E_{\text{onset}})$ .

According to the calculation, the pre-edge structure at 58 eV and the rising shoulder of the M-edge absorption at 61 eV are contributions from the tetrahedrally coordinated  $\text{Co}^{2+}$  ions, while absorption of  $\text{Co}^{3+}$  ions in octahedral sites occurs at the 64 eV peak and higher energy region. The offset between  $\text{Co}^{2+}$  and  $\text{Co}^{3+}$  absorptions helps interpret the transient XUV absorbance changes observed in the pump–probe experiment, and it further resolves which of the six band gap transition pathways the 400 nm pump pulse excites.

### 3.2 Photoinduced XUV Absorbance Changes at Cobalt M-Edge

When the thin-film  $\text{Co}_3\text{O}_4$  is pumped by 2.33  $\mu\text{J}$  energy of 400 nm light, differential absorbance changes, relative to the static spectrum, are obtained, and several of these are shown at several pump–probe temporal delays in Figure 4A. Immediately after the visible excitation, XUV absorbance has increased in the region from 59 to 66 eV with a main peak at 62.4 eV. Meanwhile decreasing XUV absorbance, that is, bleaching, appears on both sides of the positive absorbance change. From the kinetic traces at various photon energies in Figure 4B, it can be

seen that the amplitude of the transient signal reaches a maximum within 50 fs before starting to decay. The transient signal retains a similar spectral shape during the decay, and eventually, it shows no further apparent amplitude decrease out to much longer times. Experiments with pump–probe delays up to 200 ps also indicate that the transient XUV absorbance difference barely changes after the first picosecond. The transient absorption spectra are further analyzed by doing global fits with a sequential two-state model ( $A \xrightarrow{k} B$ ) with the Glotaran statistical software package.<sup>(48)</sup> Contour plots of the experimentally obtained data in the first 2 ps using 2.33  $\mu\text{J}$  pump energy and the global fit results are shown in Figure 5A and B, respectively. No characteristic residual signal remains after the fitting procedure. Convolved with a 45 fs Gaussian instrumental response function, the fit gives a  $190 \pm 10$  fs decay time constant ( $1/k$ ) from the initial excited state to a second state at this power density. The spectra of the two time-evolved excited states are shown in Figure 5C, one immediately induced by the laser pulse and one after the 190 fs decay, which lasts for at least 200 ps. Both possess very similar spectral shapes: a broad positive peak centered at 62.4 eV, with shallow, however broad bleaching on either side. One major difference between the two time-evolved spectra at the two different times is that the initial excited state undergoes a  $\sim 60\%$  decrease in amplitude after transforming to the second and longer-lived state. When normalizing the two time-evolved excited state spectra, another important experimental observation is that the positive peak in the second time-evolved state has redshifted by  $\sim 300$  meV, which is especially apparent at the higher energy shoulder.

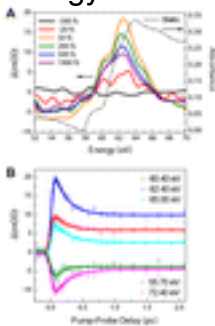


Figure 4. (A) Transient XUV spectra near the cobalt M-edge. Optical excitation is by 2.33  $\mu\text{J}$  pump energy at 400 nm wavelength. Spectra are binned by 0.1 eV and smoothed using a 2.0 eV running boxcar average. (B) Transient absorbance traces at 55.7, 60.4, 62.4, 65.0, and 72.4 eV. Points are experimental data with error bars, and solid lines are fitting results by biexponential decay equation with the longer decay component arbitrarily fixed as 300 ps, since no apparent decay is observed after 1 ps.

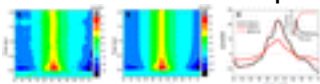


Figure 5. (A) Experimental contour plot in the first 2 ps after the pump beam

excitation. (B) Reconstructed contour plot from global fit results using a two-component sequential model. (C) Retrieved evolutionary spectra by a two-component sequential model global fit. Black solid line: the excited state A immediately after 400 nm photoexcitation. Red solid line: the long-lived state B into which the initial excited state A decays. Red dotted line: state B spectrum after being normalized to the same peak amplitude as state A. Inset: Populations of states A and B versus time. It identifies a  $190 \pm 10$  fs decay time constant ( $1/k$ ) convoluted with a 45 fs Gaussian instrumental response function.

Since the bonding character is very ionic in  $\text{Co}_3\text{O}_4$ , the electron distribution is localized and better described by orbital-like wave functions than delocalized energy bands.<sup>(19)</sup> An optical excitation can thus induce dramatic electron density redistribution at the subnanometer scale and changes of atomic oxidation states, which can be viewed as a charge transfer process. When comparing transient XUV spectra with the static  $\text{Co}_3\text{O}_4$  absorption spectrum (Figure 4A), it is clear that the positive absorbance change of excited states appears on the rising M-edge, which is mainly of  $\text{Co}^{2+}$  character. This indicates that the 400 nm excitation induces the appearance of extra  $\text{Co}^{2+}$  ions, possibly by the reduction of  $\text{Co}^{3+}$  via either LMCT or MMCT pathways. This hypothesis will be tested by more sophisticated calculations with charge transfer multiplet codes (CTM4XAS55), by comparing the experimental spectra to a simulated spectrum of each excitation pathway. The coexistence of two cobalt oxidation states ( $\text{Co}^{2+}$  and  $\text{Co}^{3+}$ ) and the oxygen anion in the spinel  $\text{Co}_3\text{O}_4$  leads to a total number of six excitation pathways as shown in Figure 1B. The oxidation state and electronic symmetry of cobalt ions in each of the tetrahedral and octahedral sites for these six excited states are listed in Table 2. LMCT processes (pathways 1 and 2) and MMCT processes (pathways 3 and 4) change both cobalt oxidation states and the electronic symmetries at one or two lattice sites, while d–d excitation pathways (5 and 6) only involve local electronic symmetry changes.

**Table 2. Cobalt Oxidation States and Electronic Symmetries at Tetrahedral and Octahedral Lattice Sites at Each Possible Excited State**

excitation pathway <sup>a</sup>	tetrahedral site		octahedral site	
	oxidation state	electronic symmetry	oxidation state	electronic symmetry
LMCT	1 1+	$^3\text{T}_1$	3+	$^1\text{A}_1$
	2 2+	$^4\text{A}_2$	2+	$^2\text{E}$
MMCT	3 1+	$^3\text{T}_1$	4+	$^2\text{T}_2$
	4 3+	$^5\text{E}$	2+	$^2\text{E}$
d–d excitation	5 2+	$^4\text{T}_2$	3+	$^1\text{A}_1$
	6 2+	$^4\text{A}_2$	3+	$^1\text{T}_1$
ground state	2+	$^4\text{A}_2$	3+	$^1\text{A}_1$

<sup>a</sup>Numbers indicating excitation pathways can be referred to Figure 1B.

Because of the spin selection rule, electronic symmetries of the two d–d excited states are assigned to the lowest excited configurations with the same spin

multiplicities on Tanabe–Sugano diagrams.<sup>(49)</sup> In most cases, electronic symmetries for different cobalt oxidation states can be determined by simply adding (or removing) one electron to (or from) the ground static electronic configurations. Ligand field splitting energies are assumed to be unchanged immediately after the optical excitation; thus, tetrahedral sites stay as high spin, and octahedral sites remain as low spin. For MMCT from  $\text{Co}^{2+}$  to  $\text{Co}^{3+}$  (pathway 4), however, an electron can be removed from either a filled  $\text{Co}^{2+} e$  orbital or a half-filled  $t_2$  orbital and put into an empty  $\text{Co}^{3+} e_g$  orbital, and the resultant electronic symmetry at the tetrahedral site could be different. Removing an electron from an  $e$  orbital would oxidize  $\text{Co}^{2+}$  to  $\text{Co}^{3+}$  and leave four unpaired electrons on cobalt (three in  $t_2$  orbitals and one in an  $e$  orbital), just like a typical high-spin tetrahedral  $d^6$  system with the most stable electronic configuration as  $^5E$ . If the electron is alternatively removed from a  $t_2$  orbital, the tetrahedral site would have a triplet  $\text{Co}^{3+}$  cation, which has only two unpaired electrons in each of the other two  $t_2$  orbitals. DFT calculation has shown that the filled minority spin  $e$  states have higher energy than majority spin  $e$  and  $t_2$  states and thus locate closer to the top of the valence band due to the spin exchange interaction.<sup>(50)</sup> As a result,  $^5E$  electronic symmetry is assigned to the tetrahedrally coordinated  $\text{Co}^{3+}$  ion after the  $\text{Co}^{2+}$  to  $\text{Co}^{3+}$  MMCT excitation.

Once each of the six possible excited states has been assigned to a set of cobalt oxidation states and electronic symmetries at two different lattice sites, their individual  $3p \rightarrow 3d$  absorption spectra are calculated with charge transfer multiplet codes by using the CTM4XAS55 program. The ground-state XUV absorption spectrum is then subtracted from each excited-state spectrum in order to be compared with the transient data acquired by pump–probe experiments. The differential spectra between each excited state and ground state are shown in Figure 6. Both LMCT excited states have XUV absorbance enhanced at lower energy and some bleaching at higher energy (Figure 6A). This can be explained by the decrease of  $3p$  electron binding energy as the cobalt oxidation number is reduced during the LMCT processes. In the same manner, the  $\text{O}^{2-}(2p) \rightarrow \text{Co}^{2+}(t_2)$  LMCT state is shifted toward lower energy compared to the  $\text{O}^{2-}(2p) \rightarrow \text{Co}^{3+}(e_g)$  LMCT state. The  $\text{Co}^{3+}(t_{2g}) \rightarrow \text{Co}^{2+}(t_2)$  MMCT state has a characteristic bleaching signal at 63 eV with two enhanced absorbance regions on either side (Figure 6B), indicating that the  $\text{Co}^{2+}(T_g)$  absorption is redshifted as it is reduced to  $\text{Co}^+$  and the  $\text{Co}^{3+}(O_h)$  absorption becomes blueshifted as it is oxidized to  $\text{Co}^{4+}$  after the MMCT excitation. As for the  $\text{Co}^{2+}(e) \rightarrow \text{Co}^{3+}(e_g)$  MMCT excited state, it can be viewed as one  $\text{Co}^{2+}$  ion exchanges its lattice symmetry with one  $\text{Co}^{3+}$  ion.

Although the stoichiometry between  $\text{Co}^{2+}/\text{Co}^{3+}$  remains at 1:2, the different lattice symmetry and spin configuration of the same metal cation can change its XUV absorption. Thus, this MMCT to form a  $\text{Co}^{3+}$  state has enhanced absorption from 64 to 68 eV. Although the amplitudes of these calculated differential spectra are somewhat arbitrary, it is clear that both d–d excited states possess only very subtle changes with respect to the ground state. As a result, the amplitudes of differential spectra of the two d–d excited states are much lower (less than 20%) compared to those of LMCT and MMCT states (Figure 6C). This is because the cobalt ions in these d–d excited states still retain the same oxidation number and spin multiplicity. An implication is that the XUV absorption spectroscopy technique might not be as sensitive to changes of d-electron configuration compared to changes of oxidation state and spin state.

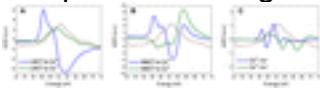


Figure 6. Differential XUV absorption spectra between ground state and calculated (A) LMCT excited states, (B) MMCT excited states, and (C) d–d excited states. Spectra in blue lines indicate  $\text{Co}^{2+}$  in a tetrahedral site receives an electron from oxygen or  $\text{Co}^{3+}$ . Spectra in green lines indicate  $\text{Co}^{3+}$  in an octahedral site receives an electron from oxygen or  $\text{Co}^{2+}$ . Experimentally obtained transient spectra of the initial excited state A (black dashed line) and the long-lived state B (red dotted line) have been normalized and overlaid with calculated spectra.

Normalized spectra of the two time-evolved excited states obtained by the global fit of the experimental results are overlapped with these calculated differential spectra, and it can be seen that the  $\text{O}^{2-}(2p) \rightarrow \text{Co}^{3+}(e_g)$  LMCT state best matches the experimental spectral shape. The enhanced absorbance at 62 eV and bleaching above 66 eV are both well reproduced, although a 500 meV to 1 eV offset might exist between the calculation and the experimental data. An excellent match between the calculated spectrum and the experimental data is not expected here for two reasons. First, these charge transfer multiplet codes have been widely used to investigate the influence of local lattice symmetry and bonding character to XUV or X-ray absorption of transition-metal-based material in the ground state. In this study, although oxidation states and electronic symmetries of cobalt ions at each excited state have been carefully assigned, the XUV absorption spectra are still calculated in the same manner as treating ground-state spectra. Many phenomena that exist in optically excited states, such as hot electrons and lattice structure rearrangement, are entirely neglected in the calculation. The interaction between the core-hole and the photogenerated hole in the valence band is also not included. It is possible that once charge transfer happens, the ligand field splitting energy for the reduced/oxidized cobalt ions might have some instantaneous changes that are not considered in the current level of calculation. The second reason that the calculation does not match

experimental spectra perfectly is that the calculated spectra at each lattice symmetric site are broadened by the same increasing Lorentzian line width formula  $\Gamma = L_{\min} + dL^*(E - E_{\text{onset}})$ , with only the onset energy  $E_{\text{onset}}$  adjusted according to the oxidation states. The fit to the experimental data can be improved if these broadening parameters can be carefully tested and adjusted for each individual excited state. In addition, the reduced absorbance from 52 to 58 eV in the transient XUV absorption spectra cannot be reproduced by the calculation. This low energy bleaching signal might correspond to the change of nonresonant absorption contribution from the ionization of cobalt 3d valence electrons but not the  $3p^6 3d^n \rightarrow 3p^5 3d^{n+1}$  core-level transitions.

After calculating differential absorbance spectra of all six possible excited states and comparing them to experimentally obtained results, it seems safe to conclude that 400 nm photoexcitation generates a  $O^{2-} \rightarrow Co^{3+}$  LMCT state in spinel  $Co_3O_4$ . This is in agreement with the previous assignments of the  $Co_3O_4$  band structure obtained theoretically(22) and experimentally,(23) namely, that the 2.8 eV absorption peak in the  $Co_3O_4$  UV/visible spectrum corresponds to the  $O^{2-}$

$(2p) \rightarrow Co^{3+}(e_g)$  transition. By comparing these findings with the current understanding of the catalytic mechanism on spinel cobalt oxide, insightful explanations for the catalytic activities of the material can be provided. For example, the  $Co_3O_4$  (110) plane is known to play a crucial role in catalytic oxidation of CO, as demonstrated both theoretically(51, 52) and experimentally.(12) Adsorption of CO onto the (110) plane occurs preferably at exposed surface  $Co^{3+}$  cations, and the subsequent abstraction of a neighboring oxygen oxidizes CO to  $CO_2$  while leaving an oxygen vacancy and a partially reduced cobalt ion in the octahedral site. As for the photocatalytic activity for the oxygen evolution half-cell reaction (OER), the  $Co_4O_4$  cubane structures formed by oxygen anions and octahedrally coordinated  $Co^{3+}$  in spinel oxides are suggested to be the active sites for the four-electron redox process,(53) due to the structural similarity between the  $Co_4O_4$  cubane and the  $CaMn_4O_x$  catalytic core in the natural photosystem II water-oxidizing complex (PSII-WOC). This work identifies that photogenerated holes in the valence band are located near oxygen atoms and might directly be involved in the OER, while electrons are near cobalt ions in octahedral lattice sites. In addition, the oxidative activity of  $Co^{3+}$  cations to be reduced to  $Co^{2+}$  could also assist the redox processes on the nearby oxygen ligands. This study first observed and assigned the photoexcited state of  $Co_3O_4$  by pumping the semiconductor material with 400 nm light. Further experiments will verify whether a different transient XUV spectrum can be observed when lower energy transitions in the UV/visible spectrum are excited.

### 3.3 Femtosecond Charge Carrier Dynamics in $Co_3O_4$

The two excited states shown in Figure 5C have similar spectral shape; one can thus assume both states possess the same  $O^{2-}(2p) \rightarrow Co^{3+}(e_g)$  charge transfer electronic character. However, the amplitude of enhanced absorption decreases for ~60% from the initial excited state to the long-lived state; also, a ~300 meV energy redshift can be observed in the long-lived state. Since the amplitude of the observed transient XUV absorbance change is proportional to the product of photogenerated charge carrier density and the transition probability change induced by each excited charge carrier, the rapid 190 fs decay can be associated with a decrease of charge carrier density near the cobalt atoms assuming the transition probability does not vary greatly. Carrier recombination can occur via both radiative and nonradiative pathways, but the time scale for carrier recombination is expected to be slower, in the nanosecond to microsecond range. On the basis of the sample absorbance at 400 nm (~0.45) and the 2.33  $\mu$ J pump energy focused to a 150  $\mu$ m spot size, a very high charge carrier density ( $8 \times 10^{21} \text{ cm}^{-3}$ ) is initially created in the  $Co_3O_4$  thin-film. This would be characterized as 0.15 charge carriers per cobalt atom. Coulomb forces among these charge carriers can lead to Auger relaxation by either an ionization or recombination mechanism in order to reduce the charge carrier density and repulsive interactions. A recent ab initio study using pseudopotential wave functions predicts that Coulomb-mediated Auger processes in spatially confined semiconductors would occur on the time scale of 100–500 fs.<sup>(54)</sup> In colloidal CdSe quantum dots,  $1P_e \rightarrow 1S_e$  electron relaxation dynamics has been measured with visible transient absorption techniques, and the 100–300 fs relaxation is believed to occur through Auger relaxation.<sup>(55, 56)</sup> Although charge carriers in thin-film  $Co_3O_4$  are not as spatially confined, an efficient Auger decay channel is still accessible due to the high charge carrier density. Another possibility for the observed subpicosecond dynamics is intersystem crossing (ISC) that commonly takes place in transition-metal complexes. Although ISC has not been well studied in solid-state metal oxides, this nonadiabatic process can occur with anomalously fast rates (tens to hundreds of femtoseconds) in transition-metal complexes in solution following an initial metal-to-ligand-charge-transfer photoexcitation,<sup>(25, 57, 58)</sup> and the resulting excited state would have a very long lifetime. For this work, it would suggest the initial  $O^{2-} \rightarrow Co^{3+}$  LMCT state undergoes subpicosecond ISC to a local d–d excited state with a different spin multiplicity. However, since the spectral shape remains almost unchanged during the 190 fs decay, it is unlikely that the electronic structure around the cobalt ions has changed dramatically, as it should with ISC. It might be possible that ISC occurs faster than the instrumental response function (45 fs) and all the observed transient XUV absorbance spectra are of the d–d excited-state character. If this is the case, then, the electronic symmetry of d–d excited states accessible by ISC is no longer limited to the two options ( ${}^4T_2$

for  $\text{Co}^{2+}$  and  $^1T_1$  for  $\text{Co}^{3+}$ , respectively) listed in Table 2. Rather, additional electronic symmetries, such as  $^2E$  and  $^2T_1$  (low spin) for  $\text{Co}^{2+}$  or  $^3T_1$  (intermediate spin) and  $^5T_2$  (high spin) for  $\text{Co}^{3+}$ , should also be considered. More sophisticated simulation of the XUV absorption of these states is required, but initial results (see Figure S5, [Supporting Information](#)) do not show that any of these local d–d states gives a better fit than the  $\text{O}^{2-} \rightarrow \text{Co}^{3+}$  LMCT state in Figure 6A. Although the intermediate-spin and high-spin d–d excited states of  $\text{Co}^{3+}$  do possess similar enhanced absorption features from 60 to 68 eV (Figure S5-B, [Supporting Information](#)), the bleaching signal above 66 eV is not reproduced as well as the simulated  $\text{O}^{2-} \rightarrow \text{Co}^{3+}$  LMCT state. Thus, the Auger relaxation is still the most likely explanation for the 190 fs rapid decay observed by the XUV probe. Since the Auger mechanism relies on the interactions between excited charge carriers, one can thus expect the Auger decay rate would increase as more charge carriers are generated by photoexcitation. The pump fluence dependence of the initial decay dynamics is studied by varying the average pump beam energy from 0.86 to 2.70  $\mu\text{J}$  (4.87 to 15.3  $\text{mJ}/\text{cm}^2$  based on a 150  $\mu\text{m}$  diameter focus size). The kinetic traces at 62.4 eV at various pump energies are shown in Figure 7A. The amplitude of the initial maximum and the plateau at a time after 1 ps both scale with the pump power used; thus, the possibility of multiphoton excitation can be excluded. However, if higher pump power is used to pump the thin-film  $\text{Co}_3\text{O}_4$  sample, the global fit gives shorter amplitude decay time constants, ranging from 269 fs at 0.86  $\mu\text{J}$  to 165 fs at 2.70  $\mu\text{J}$  (Figure 7B). The dependence of the decay rate on pump energy, or excitation density strictly speaking, suggests the Auger relaxation mechanism is responsible for the observed initial transient signal decay.

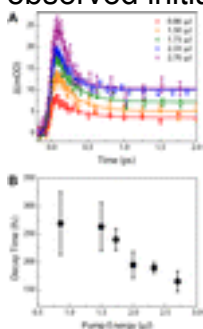


Figure 7. (A) Kinetics traces at 62.40 eV (maximum amplitude of the enhanced absorbance) as 400 nm pump beam energy varies from 0.86 to 2.70  $\mu\text{J}$ . (B) Decay time constants by global fit based on a two-component sequential model. To determine whether the 300 meV spectral shifting is associated with the 150–300 fs amplitude decay, all the transient spectra after pump–probe temporal overlap are normalized at the maximum positive amplitude. Processed dynamic traces in Figure 8 confirm that the spectral center of weight does shift to lower

energy, as the enhanced XUV absorbance gains weight on the lower energy side and loses weight on the higher energy side. However, this spectral shifting occurs with a  $535 \pm 33$  fs time constant when  $2.33 \mu\text{J}$  pump energy is used, which is slower than the 190 fs amplitude decay at the same pump energy. The same spectral redshift can still be observed at all pump energies applied, although it is difficult to determine whether the time constant associated with spectral shift also changes, or not, with different pump fluences. Nevertheless, this implies that two different carrier relaxation mechanisms might be occurring within the first 2 ps after 400 nm photoexcitation. While Auger relaxation is most likely responsible for the overall short-lived charge carrier density decay, the most likely explanation for the slower observed spectral changes is the relaxation of hot carriers via carrier–phonon interactions.

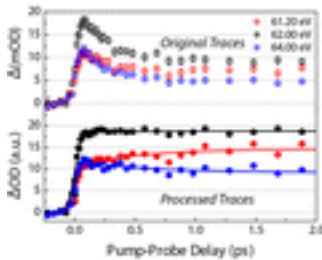


Figure 8. Top: Transient absorbance traces at 61.2, 62.0, and 64.0 eV at  $2.33 \mu\text{J}$  400 nm pump energy. Bottom: Processed traces after normalizing the maximum amplitude of every transient spectrum after the pump–probe temporal overlap. Solid lines are fitted by a two-component sequential model global fit with a 535 fs time constant.

The pump photon energy (400 nm, 3.05 eV) is higher than the direct band gap (1.6 eV); thus, photogenerated charge carriers would be formed with a significant amount of excess kinetic energy. Instantly after excitation, the system is still in a nonthermalized state: the kinetic energy distribution of carriers does not fulfill a Boltzmann distribution, and the carriers are much hotter than the lattice.

Relaxation of these “hot” carriers can occur through carrier–carrier scattering or carrier–phonon interactions.<sup>(59)</sup> Carrier relaxation on the subpicosecond time scale has been reported for CdS, another II–VI semiconductor, corresponding to Fröhlich coupling between charge carrier and longitudinal optical (LO) phonons.<sup>(60)</sup> The 535 fs spectral shift dynamics can thus be associated with the exchange of energy between the charge carriers and the lattice as the carriers undergo relaxation to the band edge. Four fundamental LO phonon frequencies have been identified for spinel  $\text{Co}_3\text{O}_4$  at 219, 394, 619, and  $683 \text{ cm}^{-1}$  (6.57, 11.8, 18.6, and  $20.5 \text{ ps}^{-1}$ , respectively),<sup>(61)</sup> indicating that, during the first 500 fs, charge carriers can effectively dissipate excess energy to the lattice by fast excitation of phonons. The charge carriers being discussed here are not limited to the electrons but can also be holes in the valence band. The  $\text{O}^{2-} (2p) \rightarrow \text{Co}^{3+} (e_g)$  charge transfer excitation creates electrons near octahedrally

coordinated cobalt cations and holes on oxygens. Although the XUV probe is sensitive only to the electronic distribution around cobalt cations, hole relaxation to the top of the valence band can also be the cause of the spectral redshift. In addition, formation of a bound electron–hole pair after hot carrier relaxation can stabilize the system and modify the XUV absorption cross section. Another possibility is that the 535 fs spectral shift of the excited state corresponds to the trapping of charge carriers on surface defect states and the lower lattice symmetry of these surface states could affect the XUV transition energies. Nevertheless, the latter case can be ruled out because trapping at surface states requires carrier diffusion and this can happen on a time scale no faster than picoseconds.

•

## 4 Conclusions

In summary, this study utilized femtosecond XUV pulses to study the photoexcited charge transfer process in mixed-valence spinel  $\text{Co}_3\text{O}_4$ , by monitoring absorbance changes at Co M-edge followed the optical excitation. Combining transient XUV spectroscopy and charge transfer multiplet calculations, the photoexcited state of thin-film  $\text{Co}_3\text{O}_4$  samples pumped by 400 nm light has been observed and assigned to the  $\text{O}^{2-}(2p) \rightarrow \text{Co}^{3+}(e_g)$  LMCT state. The few hundred femtosecond Auger relaxation immediately after photoexcitation decreases both the charge carrier density and the transient signal amplitude, and the decay rate increases as more charge carriers are generated. A 300 meV spectral redshift is caused by hot carrier relaxation to the band edge with a  $(535 \text{ fs})^{-1}$  rate constant via carrier–phonon scatterings.

### Supporting Information

Characterization of thin-film  $\text{Co}_3\text{O}_4$  samples by visible/IR absorption, selected area electron diffraction, and micro-Raman spectroscopy; spectrum of 400 nm pump pulses and extreme ultraviolet probe pulses generated by high harmonic generation. This material is available free of charge via the Internet at <http://pubs.acs.org>.

#Author Present Address

L. Robert Baker: Department of Chemistry and Biochemistry, The Ohio State University, Columbus, Ohio 43210, United States.

∇Author Present Address

J. Vura-Weis: Department of Chemistry, University of Illinois at Urbana–Champaign, Urbana, Illinois 61820, United States.

The authors declare no competing financial interest.

•

## Acknowledgment

This work is supported by the Materials Science Division of Lawrence Berkeley National Laboratory by the U.S. Department of Energy at Lawrence Berkeley

National Lab under contract no. DE-AC02-05CH11231, "Physical Chemistry of Nanomaterials." Initial work by C.-M.J. and instrument construction were supported by the NSF Engineering Research Center for Extreme Ultraviolet Science and Technology (EEC-0310717). L.R.B. and J.V.W. were supported by the U.S. Department of Defense National Security Science and Engineering Faculty Fellowship program, which is sponsored by the Office of Assistant Secretary of Defense for Research and Engineering. J.M.L. is supported as part of the Light-Material Interactions in Energy Conversion, an Energy Frontier Research Center funded by the U.S. Department of Energy, Office of Science, Office of Basic Energy Sciences, under contract no. DE-SC0001293. Brandon J. Beberwyck and Daniel J. Hellebusch are thanked for help with measurement and analysis of selected area electron diffraction data.

- [Reference QuickView](#)

- 

## References

This article references 61 other publications.

1. Goodenough, J. B. Perspective on Engineering Transition-Metal Oxides *Chem. Mater.* **2014**, 26, 820– 829 [[ACS Full Text](#) , [CAS]
2. Toroker, M. C.; Carter, E. A. Transition Metal Oxide Alloys as Potential Solar Energy Conversion Materials *J. Mater. Chem. A* **2013**, 1, 2474– 2484 [[CrossRef](#)], [CAS]
3. Poizot, P.; Laruelle, S.; Grugeon, S.; Dupont, L.; Tarascon, J. M. Nano-Sized Transition-Metal Oxides as Negative-Electrode Materials for Lithium-Ion Batteries *Nature* **2000**, 407, 496– 499 [[CrossRef](#)], [[PubMed](#)], [CAS]
4. Rockenberger, J.; Scher, E. C.; Alivisatos, A. P. A New Nonhydrolytic Single-Precursor Approach to Surfactant-Capped Nanocrystals of Transition Metal Oxides *J. Am. Chem. Soc.* **1999**, 121, 11595– 11596 [[ACS Full Text](#) , [CAS]
5. Liu, B.; Chen, H. M.; Liu, C.; Andrews, S. C.; Hahn, C.; Yang, P. Large-Scale Synthesis of Transition-Metal-Doped TiO<sub>2</sub> Nanowires with Controllable Overpotential *J. Am. Chem. Soc.* **2013**, 135, 9995– 9998 [[ACS Full Text](#) , [[PubMed](#)], [CAS]
6. Wall, S.; Foglia, L.; Wegkamp, D.; Appavoo, K.; Nag, J.; Haglund, R. F.; Stähler, J.; Wolf, M. Tracking the Evolution of Electronic and Structural Properties of VO<sub>2</sub> during the Ultrafast Photoinduced Insulator-Metal Transition *Phys. Rev. B* **2013**, 87, 115126 [[CrossRef](#)], [CAS]
7. Němec, H.; Rochford, J.; Taratula, O.; Galoppini, E.; Kužel, P.; Polívka, T.; Yartsev, A.; Sundström, V. Influence of the Electron-Cation Interaction on Electron Mobility in Dye-Sensitized ZnO and TiO<sub>2</sub> Nanocrystals: A Study Using Ultrafast Terahertz Spectroscopy *Phys. Rev. Lett.* **2010**, 104, 197401 [[CrossRef](#)], [[PubMed](#)], [CAS]

8. Thimsen, E.; Biswas, S.; Lo, C. S.; Biswas, P. Predicting the Band Structure of Mixed Transition Metal Oxides: Theory and Experiment *J. Phys. Chem. C* **2009**, 113, 2014–2021 [[ACS Full Text](#) , [CAS](#)]
9. Pastore, M.; De Angelis, F. Computational Modelling of TiO<sub>2</sub> Surfaces Sensitized by Organic Dyes with Different Anchoring Groups: Adsorption Modes, Electronic Structure and Implication for Electron Injection/recombination *Phys. Chem. Chem. Phys.* **2012**, 14, 920–928 [[CrossRef](#)], [[PubMed](#)], [[CAS](#)]
10. Zaanen, J.; Sawatzky, G. A.; Allen, J. W. Band Gaps and Electronic Structure of Transition-Metal Compounds *Phys. Rev. Lett.* **1985**, 55, 418–421 [[CrossRef](#)], [[PubMed](#)], [[CAS](#)]
11. Olalde-Velasco, P.; Jiménez-Mier, J.; Denlinger, J. D.; Hussain, Z.; Yang, W. L. Direct Probe of Mott-Hubbard to Charge-Transfer Insulator Transition and Electronic Structure Evolution in Transition-Metal Systems *Phys. Rev. B* **2011**, 83, 241102 [[CrossRef](#)], [[CAS](#)]
12. Xie, X.; Li, Y.; Liu, Z.-Q.; Haruta, M.; Shen, W. Low-Temperature Oxidation of CO Catalysed by Co<sub>3</sub>O<sub>4</sub> Nanorods *Nature* **2009**, 458, 746–749 [[CrossRef](#)], [[PubMed](#)], [[CAS](#)]
13. Park, J.-Y.; Lee, Y.-J.; Karandikar, P. R.; Jun, K.-W.; Ha, K.-S.; Park, H.-G. Fischer–Tropsch Catalysts Deposited with Size-Controlled Co<sub>3</sub>O<sub>4</sub> Nanocrystals: Effect of Co Particle Size on Catalytic Activity and Stability *Appl. Catal., A* **2012**, 411–412, 15–23 [[CrossRef](#)], [[CAS](#)]
14. Tyo, E. C.; Yin, C.; Di Vece, M.; Qian, Q.; Kwon, G.; Lee, S.; Lee, B.; DeBartolo, J. E.; Seifert, S.; Winans, R. E. Oxidative Dehydrogenation of Cyclohexane on Cobalt Oxide (Co<sub>3</sub>O<sub>4</sub>) Nanoparticles: The Effect of Particle Size on Activity and Selectivity *ACS Catal.* **2012**, 2, 2409–2423 [[ACS Full Text](#) , [[CAS](#)]
15. Jiao, F.; Frei, H. Nanostructured Cobalt Oxide Clusters in Mesoporous Silica as Efficient Oxygen-Evolving Catalysts *Angew. Chem., Int. Ed.* **2009**, 48, 1841–1844 [[CrossRef](#)], [[PubMed](#)], [[CAS](#)]
16. Gasparotto, A.; Barreca, D.; Bekermann, D.; Devi, A.; Fischer, R. A.; Fornasiero, P.; Gombac, V.; Lebedev, O. I.; Maccato, C.; Montini, T. F-Doped Co<sub>3</sub>O<sub>4</sub> Photocatalysts for Sustainable H<sub>2</sub> Generation from Water/Ethanol *J. Am. Chem. Soc.* **2011**, 133, 19362–19365 [[ACS Full Text](#) , [[PubMed](#)], [[CAS](#)]
17. Zou, X.; Su, J.; Silva, R.; Goswami, A.; Sathe, B. R.; Asefa, T. Efficient Oxygen Evolution Reaction Catalyzed by Low-Density Ni-Doped Co<sub>3</sub>O<sub>4</sub> Nanomaterials Derived from Metal-Embedded Graphitic C<sub>3</sub>N<sub>4</sub> *Chem. Commun.* **2013**, 49, 7522–7524 [[CrossRef](#)], [[PubMed](#)], [[CAS](#)]
18. Haneda, M.; Kintaichi, Y.; Bion, N.; Hamada, H. Alkali Metal-Doped Cobalt Oxide Catalysts for NO Decomposition *Appl. Catal., B* **2003**, 46, 473–482 [[CrossRef](#)], [[CAS](#)]

19. Chen, J.; Wu, X.; Selloni, A. Electronic Structure and Bonding Properties of Cobalt Oxide in the Spinel Structure *Phys. Rev. B* **2011**, *83*, 245204[CrossRef], [CAS]
20. Bai, L.; Pravica, M.; Zhao, Y.; Park, C.; Meng, Y.; Sinogeikin, S. V.; Shen, G. Charge Transfer in Spinel  $\text{Co}_3\text{O}_4$  at High Pressures *J. Phys.: Condens. Matter* **2012**, *24*, 435401[CrossRef], [PubMed], [CAS]
21. Ruzakowski Athey, P.; Urban, F. K., III; Tabet, M. F.; McGahan, W. A. Optical Properties of Cobalt Oxide Films Deposited by Spray Pyrolysis *J. Vac. Sci. Technol., A* **1996**, *14*, 685– 692[CrossRef]
22. Miedzinska, K. M. E.; Hollebhone, B. R.; Cook, J. G. An Assignment of the Optical Absorption Spectrum of Mixed Valence  $\text{Co}_3\text{O}_4$  Spinel Films *J. Phys. Chem. Solids* **1987**, *48*, 649– 656[CrossRef], [CAS]
23. Kim, K. J.; Park, Y. R. Optical Investigation of Charge-Transfer Transitions in Spinel  $\text{Co}_3\text{O}_4$  *Solid State Commun.* **2003**, *127*, 25– 28[CrossRef], [CAS]
24. Van der Laan, G. M. <sub>2,3</sub> Absorption Spectroscopy of 3d Transition-Metal Compounds *J. Phys.: Condens. Matter* **1991**, *3*, 7443– 7454[CrossRef], [CAS]
25. Huse, N.; Cho, H.; Hong, K.; Jamula, L.; de Groot, F. M. F.; Kim, T. K.; McCusker, J. K.; Schoenlein, R. W. Femtosecond Soft X-Ray Spectroscopy of Solvated Transition-Metal Complexes: Deciphering the Interplay of Electronic and Structural Dynamics *J. Phys. Chem. Lett.* **2011**, *2*, 880– 884[ACS Full Text , [PubMed], [CAS]
26. Qiao, R.; Chin, T.; Harris, S. J.; Yan, S.; Yang, W. Spectroscopic Fingerprints of Valence and Spin States in Manganese Oxides and Fluorides *Curr. Appl. Phys.* **2013**, *13*, 544– 548[CrossRef]
27. Corkum, P. B. Plasma Perspective on Strong Field Multiphoton Ionization *Phys. Rev. Lett.* **1993**, *71*, 1994– 1997[CrossRef], [PubMed], [CAS]
28. Hosler, E. R.; Leone, S. R. Characterization of Vibrational Wave Packets by Core-Level High-Harmonic Transient Absorption Spectroscopy *Phys. Rev. A* **2013**, *88*, 023420[CrossRef], [CAS]
29. Lin, M.-F.; Neumark, D. M.; Gessner, O.; Leone, S. R. Ionization and Dissociation Dynamics of Vinyl Bromide Probed by Femtosecond Extreme Ultraviolet Transient Absorption Spectroscopy *J. Chem. Phys.* **2014**, *140*, 064311[CrossRef], [CAS]
30. Loh, Z.; Leone, S. R. Capturing Ultrafast Quantum Dynamics with Femtosecond and Attosecond X-Ray Core-Level Absorption Spectroscopy *J. Phys. Chem. Lett.* **2013**, *4*, 292– 302[ACS Full Text , [CAS]
31. Goulielmakis, E.; Loh, Z.-H.; Wirth, A.; Santra, R.; Rohringer, N.; Yakovlev, V. S.; Zherebtsov, S.; Pfeifer, T.; Azzeer, A. M.; Kling, M. F. Real-Time Observation of Valence Electron Motion *Nature* **2010**, *466*, 739– 743[CrossRef], [PubMed], [CAS]

32. Schultze, M.; Bothschafter, E. M.; Sommer, A.; Holzner, S.; Schweinberger, W.; Fiess, M.; Hofstetter, M.; Kienberger, R.; Apalkov, V.; Yakovlev, V. S. Controlling Dielectrics with the Electric Field of Light *Nature* **2013**, 493, 75–78 [[CrossRef](#)], [[PubMed](#)], [[CAS](#)]
33. Hillyard, P. W.; Kuchibhatla, S. V. N. T.; Glover, T. E.; Hertlein, M. P.; Huse, N.; Nachimuthu, P.; Saraf, L. V.; Thevuthasan, S.; Gaffney, K. J. Atomic Resolution Mapping of the Excited-State Electronic Structure of  $\text{Cu}_2\text{O}$  with Time-Resolved X-Ray Absorption Spectroscopy *Phys. Rev. B* **2009**, 80, 125210 [[CrossRef](#)], [[CAS](#)]
34. Chen, L. X.; Zhang, X.; Lockard, J. V.; Stickrath, A. B.; Attenkofer, K.; Jennings, G.; Liu, D.-J. Excited-State Molecular Structures Captured by X-Ray Transient Absorption Spectroscopy: A Decade and Beyond *Acta Crystallogr., Sect. A: Found. Crystallogr.* **2010**, 66, 240–251 [[CrossRef](#)], [[PubMed](#)], [[CAS](#)]
35. Lima, F. A.; Milne, C. J.; Amarasinghe, D. C. V.; Rittmann-Frank, M. H.; van der Veen, R. M.; Reinhard, M.; Pham, V.-T.; Karlsson, S.; Johnson, S. L.; Grolimund, D. A High-Repetition Rate Scheme for Synchrotron-Based Picosecond Laser Pump/x-Ray Probe Experiments on Chemical and Biological Systems in Solution *Rev. Sci. Instrum.* **2011**, 82, 063111 [[CrossRef](#)], [[CAS](#)]
36. Canton, S. E.; Zhang, X.; Zhang, J.; van Driel, T. B.; Kjaer, K. S.; Haldrup, K.; Chabera, P.; Harlang, T.; Suarez-Alcantara, K.; Liu, Y. Toward Highlighting the Ultrafast Electron Transfer Dynamics at the Optically Dark Sites of Photocatalysts *J. Phys. Chem. Lett.* **2013**, 4, 1972–1976 [[ACS Full Text](#)], [[PubMed](#)], [[CAS](#)]
37. Boeglin, C.; Beaurepaire, E.; Halté, V.; López-Flores, V.; Stamm, C.; Pontius, N.; Dürr, H. A.; Bigot, J.-Y. Distinguishing the Ultrafast Dynamics of Spin and Orbital Moments in Solids *Nature* **2010**, 465, 458–461 [[CrossRef](#)], [[PubMed](#)], [[CAS](#)]
38. Papalazarou, E.; Boschetto, D.; Gautier, J.; Garl, T.; Valentin, C.; Rey, G.; Zeitoun, P.; Rousse, A.; Balcou, P.; Marsi, M. Probing Coherently Excited Optical Phonons by Extreme Ultraviolet Radiation with Femtosecond Time Resolution *Appl. Phys. Lett.* **2008**, 93, 41114 [[CrossRef](#)], [[CAS](#)]
39. Turgut, E.; La-o-vorakiat, C.; Shaw, J. M.; Grychtol, P.; Nembach, H. T.; Rudolf, D.; Adam, R.; Aeschlimann, M.; Schneider, C. M.; Silva, T. J. Controlling the Competition between Optically Induced Ultrafast Spin-Flip Scattering and Spin Transport in Magnetic Multilayers *Phys. Rev. Lett.* **2013**, 110, 197201 [[CrossRef](#)], [[PubMed](#)], [[CAS](#)]
40. Vura-Weis, J.; Jiang, C.-M.; Liu, C.; Gao, H.; Lucas, J. M.; de Groot, F. M. F.; Yang, P.; Alivisatos, A. P.; Leone, S. R. Femtosecond  $M_{2,3}$ -Edge Spectroscopy of Transition-Metal Oxides: Photoinduced Oxidation State Change in  $\text{A-Fe}_2\text{O}_3$  *J. Phys. Chem. Lett.* **2013**, 4, 3667–3671 [[ACS Full](#)]

Text , [CAS]

41. The Center for X-ray Optics Home Page. <http://www.cxro.lbl.gov/>.
42. Tang, C.-W.; Wang, C.-B.; Chien, S.-H. Characterization of Cobalt Oxides Studied by FT-IR, Raman, TPR and TG-MS *Thermochim. Acta* **2008**, 473, 68– 73[CrossRef], [CAS]
43. Brichta, J.-P.; Wong, M. C. H.; Bertrand, J. B.; Bandulet, H.-C.; Rayner, D. M.; Bhardwaj, V. R. Comparison and Real-Time Monitoring of High-Order Harmonic Generation in Different Sources *Phys. Rev. A* **2009**, 79, 33404[CrossRef], [CAS]
44. Stavitski, E.; de Groot, F. M. F. The CTM4XAS Program for EELS and XAS Spectral Shape Analysis of Transition Metal L Edges *Micron* **2010**, 41, 687– 694[CrossRef], [PubMed], [CAS]
45. Ikeno, H.; de Groot, F. M. F.; Stavitski, E.; Tanaka, I. Multiplet Calculations of  $L_{2,3}$  X-Ray Absorption near-Edge Structures for 3d Transition-Metal Compounds *J. Phys.: Condens. Matter* **2009**, 21, 104208[CrossRef], [PubMed], [CAS]
46. Morales, F.; de Groot, F. M. F.; Glatzel, P.; Kleimenov, E.; Bluhm, H.; Hävecker, M.; Knop-Gericke, A.; Weckhuysen, B. M. In Situ X-Ray Absorption of Co/Mn/TiO<sub>2</sub> Catalysts for Fischer–Tropsch Synthesis *J. Phys. Chem. B* **2004**, 108, 16201– 16207[ACS Full Text , [CAS]
47. Taguchi, M.; Uozumi, T.; Kotani, A. Theory of X-Ray Photoemission and X-Ray Emission Spectra in Mn Compounds *J. Phys. Soc. Jpn.* **1997**, 66, 247– 256[CrossRef], [CAS]
48. Valero-Mora, P. M.; Ledesma, R. D. Graphical User Interfaces for R *J. Stat. Software* **2012**, 49, 1– 8
49. Tanabe, Y.; Sugano, S. On the Absorption Spectra of Complex Ions II *J. Phys. Soc. Jpn.* **1954**, 9, 766– 779[CrossRef], [CAS]
50. Walsh, A.; Wei, S.-H.; Yan, Y.; Al-Jassim, M. M.; Turner, J. A.; Woodhouse, M.; Parkinson, B. A. Structural, Magnetic, and Electronic Properties of the Co-Fe-Al Oxide Spinel System: Density-Functional Theory Calculations *Phys. Rev. B* **2007**, 76, 165119[CrossRef], [CAS]
51. Broqvist, P.; Panas, I.; Persson, H. A DFT Study on CO Oxidation over Co<sub>3</sub>O<sub>4</sub> *J. Catal.* **2002**, 210, 198– 206[CrossRef], [CAS]
52. Jiang, D.; Dai, S. The Role of Low-Coordinate Oxygen on Co<sub>3</sub>O<sub>4</sub> (110) in Catalytic CO Oxidation *Phys. Chem. Chem. Phys.* **2011**, 13, 978– 984[CrossRef], [PubMed], [CAS]
53. Gardner, G. P.; Go, Y. B.; Robinson, D. M.; Smith, P. F.; Hadermann, J.; Abakumov, A.; Greenblatt, M.; Dismukes, G. C. Structural Requirements in Lithium Cobalt Oxides for the Catalytic Oxidation of Water *Angew. Chem., Int. Ed.* **2012**, 51, 1616– 1619[CrossRef], [PubMed], [CAS]
54. Wang, L.-W.; Califano, M.; Zunger, A.; Franceschetti, A. Pseudopotential Theory of Auger Processes in CdSe Quantum Dots *Phys. Rev. Lett.* **2003**, 91, 056404[CrossRef], [CAS]

55. Klimov, V. I.; McBranch, D. W. Femtosecond 1P-to-1S Electron Relaxation in Strongly Confined Semiconductor Nanocrystals *Phys. Rev. Lett.* **1998**, 80, 4028– 4031[[CrossRef](#)], [[CAS](#)]
56. Cooney, R. R.; Sewall, S. L.; Dias, E. A.; Sagar, D. M.; Anderson, K. E. H.; Kambhampati, P. Unified Picture of Electron and Hole Relaxation Pathways in Semiconductor Quantum Dots *Phys. Rev. B* **2007**, 75, 245311[[CrossRef](#)], [[CAS](#)]
57. Gawelda, W.; Cannizzo, A.; Pham, V.-T.; van Mourik, F.; Bressler, C.; Chergui, M. Ultrafast Nonadiabatic Dynamics of  $[\text{Fe}^{\text{II}}(\text{bpy})_3]^{2+}$  in Solution *J. Am. Chem. Soc.* **2007**, 129, 8199– 8206[[ACS Full Text](#) , [[PubMed](#)], [[CAS](#)]
58. Chou, P.-T.; Chi, Y.; Chung, M.-W.; Lin, C.-C. Harvesting Luminescence via Harnessing the Photophysical Properties of Transition Metal Complexes *Coord. Chem. Rev.* **2011**, 255, 2653– 2665[[CrossRef](#)], [[CAS](#)]
59. Klimov, V. I. Optical Nonlinearities and Ultrafast Carrier Dynamics in Semiconductor Nanocrystals *J. Phys. Chem. B* **2000**, 104, 6112– 6123[[ACS Full Text](#) , [[CAS](#)]
60. Klimov, V.; Haring Bolivar, P.; Kurz, H. Hot-Phonon Effects in Femtosecond Luminescence Spectra of Electron-Hole Plasmas in CdS *Phys. Rev. B* **1995**, 52, 4728– 4731[[CrossRef](#)], [[PubMed](#)], [[CAS](#)]
61. Lenglet, M.; Lefez, B. Infrared Optical Properties of Cobalt (II) Spinels *Solid State Commun.* **1996**, 98, 689– 694[[CrossRef](#)], [[CAS](#)]